

Facile Synthesis of Hierarchical CuS and CuCo₂S₄ Structures from an Ionic Liquid Precursor for Electrocatalysis Applications

Ahed Abouserie,^{§[a]} Gumaa A. El-Nagar,^{*§[b, f, g]} Benjamin Heyne,^[d] Christina Günter,^[e, g] Uwe Schilde,^[a] Matthew T. Mayer,^[f] Sasho Stojkovic,^{f, g} Christina Roth,^[c] and Andreas Taubert^{*[a]}

^aInstitute of Chemistry, University of Potsdam, D-14476 Potsdam, Germany

^bDepartment of Chemistry, Faculty of Science, Cairo University, 12613, Giza, Egypt

^cMaterials Process Engineering, Faculty of Engineering University of Bayreuth, 95447 Bayreuth, Germany

^dFraunhofer Institute for Applied Polymer Research Potsdam-Golm, D-14476 Potsdam, Germany

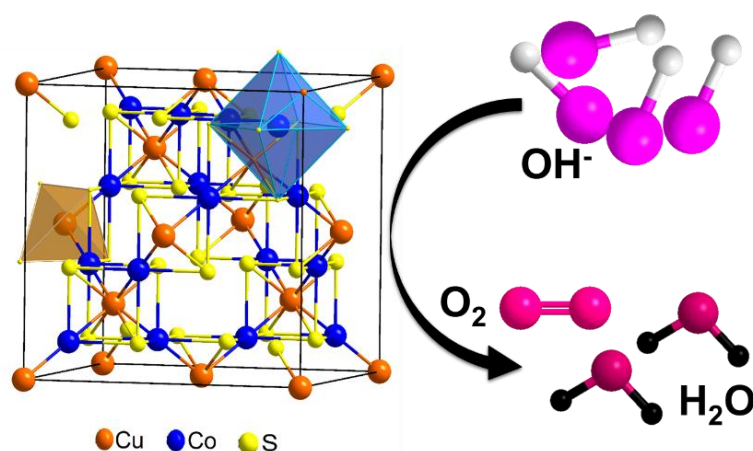
^eInstitute of Geosciences, University of Potsdam, D-14476 Potsdam, Germany

^fYoung investigator group: Electrochemical Conversion of CO₂, Helmholtz-Zentrum Berlin für Materialien und Energie, 14109 Berlin - Germany

^gInstitut für Chemie & Biochemie Physikalische & Theoretische Chemie, Freie Universität Berlin, D-14195, Berlin, Germany

Abstract

Covellite phase CuS and carrollite phase CuCo₂S₄ nano- and microstructures were synthesized from tetrachloridometallate-based ionic liquid precursors using a novel, facile, and highly controllable hot-injection synthesis strategy. The synthesis parameters including reaction time and temperature were first optimized to produce CuS with a well-controlled and unique morphology providing the best electrocatalytic activity towards the oxygen evolution reaction (OER). In an extension to this approach, the electrocatalytic activity was further improved by incorporating Co in the CuS synthesis method to yield CuCo₂S₄ microflowers synthesized via the same approach. Both routes provide high microflower yields of >80 wt.%. The CuCo₂S₄ microflowers exhibit a superior performance for the OER in alkaline medium compared to CuS. This is demonstrated by a lower onset potential (~1.45 V vs. RHE @10 mA/cm²), better durability, and higher turnover frequencies compared to bare CuS flowers or commercial Pt/C and IrO₂ electrodes. Likely, this effect is associated with the presence of Co³⁺ sites on which a better adsorption of reactive species formed during OER (e.g., OH, O, OOH, etc.) can be achieved, thus reducing the OER charge transfer resistance, as indicated from XPS and EIS measurements.



Keywords: oxygen evolution reaction, nanoparticles, copper cobalt sulfide, ionic liquid, water splitting

* Corresponding authors: G. A. El-Nagar (Gumaa.el-nagar@helmholtz-berlin.de) & A. Taubert (ataubert@uni-potsdam.de).[§] Shared first author and contributed equally

1. Introduction

The world's growing energy demand in conjunction with environmental issues originating from the widespread use of fossil fuels have led to a tremendous push towards alternative, clean, and sustainable energy sources worldwide.¹ Catalytic water splitting is among the most prominent approaches towards sustainable fuel production. However, several obstacles exist. Most prominently, the sluggish kinetics (i.e., high overpotential) of the oxygen evolution reaction (OER) is a key bottleneck in electrocatalytic water splitting. RuO₂ and IrO₂ are the current state-of-the-art catalysts for efficient OER at low overpotential; their high cost and limited availability, however, drastically restrict their application on a larger scale.²⁻³ Consequently, there is a rather urgent need for cheap, robust, and highly effective electrocatalysts for application in OER systems. As a result, numerous efforts have been dedicated to non-precious materials, including transition metal oxides, perovskites, chalcogenides, nitrides, hydroxides, and phosphides.⁴⁻⁶

In spite of these significant efforts, the performance of these non-precious metal-based electrocatalysts is significantly lower in comparison with the expensive and high-performance water oxidation electrocatalysts.⁷⁻⁸ Moreover, many of these non-noble catalysts have drawbacks such as lower stability under real-device conditions, lower number of active sites, poor electron transfer, and poor contact with the electrolyte. Thus, there is an urgent need for facile, cheap, and efficient approaches towards OER electrocatalysts with high stability and high activity. Among others, ionic liquids (ILs) and ionic liquid precursors (ILPs) may provide such suitable synthetic approaches.⁹⁻¹²

ILs are organic compounds that consist of completely from ions, with relatively low melting point. Their properties can be tuned by an appropriate choice of the cation and the anion. ILs have received much attention over the last decades covering many fields due to their remarkable properties including very low vapor pressure, high ionic conductivity, low melting points, and so forth. Of particular interest to the current study, metal-containing ILs (MILs) have been used as ILPs for inorganic nanomaterials

synthesis, where the ILP acts at the same time as the solvent, the template, and the precursor (providing at least one component) of the inorganic material.¹³ For instance, the ILP approach has been used for preparation of various inorganic materials including CuCl⁹, Au¹⁴, (doped) carbon materials¹⁵⁻¹⁶, Ni and NiO nanomaterials¹⁷⁻¹⁸, CuS¹², Fe₃C¹⁹, In₂O₃²⁰, ZnO²¹, CuO²², and metal fluorides.²³⁻²⁴ Although ILs are still somewhat more expensive than conventional solvents, they have clear advantages as outlined above. Moreover, there are sustainable synthesis protocols available suggesting that cost will not be a decisive factor in using ILs in the future²⁵⁻²⁷.

Transition metal chalcogenides, especially sulfides, have attracted significant attention due to their excellent electrical, optical, and catalytic properties.²⁸⁻²⁹ Accordingly, transition metal chalcogenides have found application in many fields including lithium-ion batteries³⁰ and , water splitting.³¹ Copper sulfide³² and cobalt sulfide³³ are among the most important chalcogenides in this context.

CuS stoichiometry, structure, shape, and Cu oxidation state could be used for tuning their electrochemical and physical properties. Accordingly, Cu_{2-x}S (x =0-1) with different composition and morphologies including covellite (CuS), anilite (Cu_{1.75}S)³⁴, digenite (Cu_{1.8}S)³⁵, djurleite (Cu_{1.96}S)³⁶, and chalcocite (Cu₂S)³⁷ have been synthesized. In this regard, various synthesis strategies such as solvothermal synthesis, hot-injection solution synthesis, sonochemical synthesis , chemical vapor deposition and vapor-liquid-solid growth have been introduced to construct CuS nanostructures.³⁸⁻³⁹ Nevertheless, the preparation of CuS particles with a well-defined and controlled features including particle size, shape, stoichiometry, hierarchical organization, and defined crystal structure via a scalable, easy, and cheap synthetic approach is still a challenge.⁴⁰⁻⁴¹

Additionally, electrochemical applications often benefit from non-stoichiometric compositions, solid solution-type materials composition, or effects of doping certain elements into an existing lattice. Often, however, these systems are difficult to synthesize because they are thermodynamically unstable and are driven towards phase separation yielding a two-component solid material or powder rather than the

desired product, e.g. a solid solution. Although there are numerous strategies available for the synthesis of well-defined (inorganic) nanomaterials, there is a need to further evaluate protocols that enable the fabrication of materials with specific and often uncommon compositions without driving the system into phase separation.

Mixed-metal sulfides such as copper-cobalt sulfides further expand the chemical and physical properties provided by the single metal counterparts. For example, Li et al.⁴² synthesized Co-doped Cu_7S_4 nanodisks via fast thermolysis and showed that the introduction of traces of cobalt into the Cu_7S_4 lattice greatly enhances the OER performance. Meenakshi et al.⁴³ reported that the replacement of some of the cobalt(II) ions in the tetrahedral sites of Co_3S_4 with copper(II) ions results in the formation of CuCo_2S_4 carrollite with a standard spinel structure which is paramagnetic and metallic in its bulk. Generally, the octahedral Co(III) sites of the spinel structure are catalytically active, while the tetrahedral Cu(II) sites (divalent copper sites) are almost inactive.⁴³⁻⁴⁴ Thus, there is an interest in multicomponent metal sulfides and well-designed synthesis protocols enabling the controlled synthesis of such materials with controlled composition and morphology. Tang et al.⁴⁵ fabricated CuCo_2S_4 nanostructures via a solvothermal reaction with superior performance in supercapacitor applications. Wiltrout et al.⁴⁶ synthesized colloidal CuCo_2S_4 nanoparticles using a solution approach.

We have recently established the concept of ILPs for the synthesis of inorganic nanomaterials including CuCl^9 , Fe_3C^{19} , and a few other materials with high application potential.⁴⁷⁻⁴⁸ The current article expands this ever growing, highly flexible and adaptable platform of ILPs and demonstrates for the first time that ILPs also provide rapid and highly reproducible access to materials for electrochemical applications such as water splitting. The current report demonstrates for the first time that precisely defined ILPs containing more than one metal are viable precursors for the direct one-step synthesis of multi-metal sulfides such as carrollite nanomaterials. The ILP used in the current work is based on the tetrachloridometallate(II) anion, where the metal center within the tetrachloridometallate(II) anion is

Cu(II) and Co(II), and the N-butylpyridinium (C_4Py) cation is the counterion. The ILP used here has the composition $[C_4Py]_2[Cu_{0.39}Co_{0.61}Cl_4]$. The $CuCo_2S_4$ microflowers obtained from reaction of the ILP with a sulfur source exhibit outstanding OER activity and excellent stability with overall performance comparable to or higher than that of the other transition metal chalcogenides reported so far, especially when compared to the pure CuS or Co_3S_4 microflowers.

1. Experimental

1.1. Chemicals

N-butylpyridinium chloride (IoLiTec, 99%), bis(trimethylsilyl) sulfide ($(TMS)_2S$, Sigma-Aldrich, 99%), $CuCl_2 \cdot 2H_2O$ (Fluka, $\geq 99\%$), $Na_2HPO_4 \cdot 7H_2O$ (Sigma-Aldrich, $\geq 99.99\%$), $CoCl_2 \cdot 6H_2O$ (Ucb, 98%), acetonitrile (Sigma-Aldrich, 99.8%), isopropanol (Sigma-Aldrich, 99.7%), and Nafion (5 wt.%, Sigma-Aldrich) were used to prepare CuS microstructures and were used as received without further purifications. All solutions used in this study were freshly prepared using Milli-Q water (18.2 M Ω cm).

1.2. Synthesis of CuS microflowers

The ILP $[C_4Py]_2[CuCl_4]$ was prepared as previously described elsewhere.⁴⁹ The final CuS particles were prepared using a hot-injection process in argon atmosphere. Briefly, 1 mmol (0.478 g) of $[C_4Py]_2[CuCl_4]$ was first heated to 160 °C, followed by a rapid adding of 1 mmol (0.211 mL) of $(TMS)_2S$ via a syringe. The orange color of the liquid instantly converted into black and supplemented with the precipitation of CuS particles with the injection. Next, the reaction mixture was kept under vigorous stirring at 160 °C for 1 hour followed by a cooling step to room temperature. Then, the dark brown to black CuS particles were collected and cleaned by repetitive cycles of washing/centrifugation with absolute ethanol and milli-Q water. Lastly, the obtained CuS particles were dried for 12 hours under

vacuum at room temperature. To obtain CuS particles with various shapes and crystal structures, different reaction times (between 1 and 8 h) and temperatures (between 120 and 200 °C) were used.

1.3. Synthesis of bis(N-butylpyridinium) tetrachloridocuprate(II)cobaltate(II)

The ILP was synthesized as described elsewhere.⁵⁰ In short, 1.5 mmol CuCl₂ (0.258 g) and 1.5 mmol CoCl₂ (0.357 g) were added into in 6 ml dry acetonitrile containing 6 mmol N-butylpyridinium chloride. This mixture was stirred for 3 hours at reflux. Rotary evaporation was used to remove the solvent at 60 °C under lowered pressure and the obtained product was next dried under vacuum. Yield: 1.40 g (98 wt. %).

Elemental analysis (CHN analysis, described below in section 2.5) for C₁₈H₂₈Cl₄Cu_{0.39}Co_{0.61}N₂ calculated (found): C, 45.52 wt.% (45.03%); H, 5.94 wt.% (6.12%); N, 5.9 wt.% (5.92%). ICP-OES (described below in section 2.5): Cu 5.04 wt%, Co 7.50 wt%. MS (positive mode): m/z = 136.1123 [C₉H₁₄N]⁺. This compound is hereafter referred to as [C₄Py]₂[Cu_{0.39}Co_{0.61}Cl₄].

1.4. Synthesis of CuCo₂S₄ Microflowers

CuCo₂S₄ microflowers were obtained using a hot-injection strategy in argon atmosphere as follows¹²: 2 mmol (0.422 mL) of (TMS)₂S were added into preheated 0.5 mmol (0.237 g) of [C₄Py]₂[Cu_{0.39}Co_{0.61}Cl₄] at 180 °C using a syringe. Upon injection, the green color of this mixture immediately transformed to black together with precipitation of a dark solid particles. This reaction mixture was kept for 6 hours under vigorous stirring at 180 °C and then cooled to room temperature. After this cooling step, the resulting dark brown to black precipitate was collected and cleaned by repeated cycles of washing/centrifugation with absolute ethanol and mill-Q water. Finally, the obtained particles were dried for 12 hours at room temperature under vacuum. 127.8 mg of CuCo₂S₄ powder (83 wt.% yield) was obtained at the end.

1.5. Apparatus

Elemental Analysis (CHN) was examined by an Elementar vario EL III analyzer with 0.3 wt.% detection limit.

Inductively Coupled Plasma (ICP) spectroscopy was carried out at the Mikroanalytisches Labor Kolbe, Mülheim, Germany. A Perkin Elmer Analyst 200 Atomic Absorption spectrometer was used to determine the metal contents.

Mass Spectrometry (MS) was conducted by a Micromass quadrupole – time of flight (QTOF) mass spectrometer with an electrospray ionization (ESI) source operated in positive ionization mode, with an m/z range of 50-800. Diluted methanol solutions of the prepared materials were injected.

Differential Scanning Calorimetry (DSC) measurements were performed with a Netzsch DSC 214 Polyma in nitrogen environment. The provided aluminum pans with a pierced lid by DSC manufacturer was used as sample holder. Three heating and cooling cycles in the range of -100 to 150 °C at 10 °C min⁻¹ were employed in the DSC measurements. Isothermal time between cooling and heating cycles was 10 min.

Single crystal structure analysis was done as follows: A suitable single crystal of [C₄Py]₂[Cu_{0.39}Co_{0.61}Cl₄], which was grown by diffusion of methyl tert-butyl ether vapor into an ethanolic solution of the compound, was embedded in perfluoropolyalkylether oil and mounted within a MicroGripper. The data collection was carried out at 210 K on a STOE StadiVari diffractometer equipped with a four-circle goniometer (open Eulerian cradle), a Genix Microfocus X-ray source (Mo) with a graded multilayer mirror and a Dectris 200 K detector ($\Delta\omega=0.5^\circ$; detector distance 60 mm; 2017 frames, 15 s exposure time per frame). All the obtained data were corrected for both Lorentz and polarization effects. Numerical absorption corrections were applied using optimized shape⁵¹. The structure was solved by direct methods using the program SHELXS-2013/1⁵² and refined against F^2 by means of full-matrix least-squares procedures using the program SHELXL-2014/7.⁵³ Non-hydrogen atoms were refined with anisotropic temperature factors. The hydrogen atoms were calculated in their expected positions and refined using a riding model with C–H = 0.94 Å (–CH), C–H = 0.98 Å (–CH₂) and C–H = 0.97 Å (–CH₃), allowing for rotation), and $U_{\text{iso}}(\text{H}) = 1.2U_{\text{eq}}(\text{CH}, \text{CH}_2)$ and $U_{\text{iso}}(\text{H}) =$

1.5U_{eq}(CH₃). For visualization, the programs DIAMOND⁵⁴ and ORTEP⁵⁵ were used. CCDC 1999142 contains the supplementary crystallographic data for this paper. These data can be obtained free of charge from The Cambridge Crystallographic Data Centre via <https://www.ccdc.cam.ac.uk/structures/>. Powder patterns calculated from the single crystal data exactly match the powder diffraction data from the as-synthesized compound [C₄Py]₂[Cu_{0.39}Co_{0.61}Cl₄] – the single crystal structure of the compound is thus identical to the structure of the powders

Powder X-ray Diffraction (XRD) of the prepared materials was examined by a PANalytical Empyrean with Bragg-Brentano geometry and PIXcel1D detector using Cu K_α radiation (λ = 1.5419 Å). The instrument was operated at 40 kV and 40 mA over 2θ range of 4–70° with 0.0131° step size and 1s sample rotation time for 190 min. PHD Level of the detector was set to 45–80 to reduce the fluorescence. The average crystallite sizes D were calculated through the Scherrer equation.⁵⁶

$$D = K\lambda / (\beta \cos \theta)$$

where *K* is the Scherrer constant (0.9), λ is the wavelength of X-ray radiation (λ = 1.5419 Å), β is the full-width-at-half-maximum of the (012) and (113) reflections, and θ is their respective position.

Scanning Electron Microscopy (SEM) was performed on a JEOL JSM-6510 (W cathode, 15 kV) equipped with Oxford Instruments INCA x-act detector to measure *energy dispersive X-ray spectroscopy* (EDXS) unit. Samples were mounted on an aluminum stub with adhesive carbon tape and coated with carbon using a Polaron CC7650 Carbon Coater. Additionally, the elemental EDX mapping was conducted using a Zeiss UltraPlus Scanning Electron Microscope with EDX detector from Thermo Fisher at acceleration voltage of 20 kV.

X-ray photoelectron spectroscopy (XPS, Axis165, Kratos Analytical, Al K_α X-ray source), was used to determine the surface elemental composition of the samples. For evaluation, a linear background was first subtracted, and peaks were fitted with gaussian shapes with equal FWHM for the

same species. The fitted peaks of were assigned to the most plausible assignment according to literature.

Electrochemical analysis was performed on a typical three-electrode setup GAMRY Potentiostat/Galvanostat (Reference 600). A piece of carbon paper with 1 cm² geometric surface area modified with the catalyst materials acted as working electrode, while a spiral Pt wire and saturated standard calomel (SCE) served as counter and reference electrodes, respectively. The measured potential against SCE then converted to RHE using the standard equation ($E_{\text{RHE}} = E_{\text{SCE}} + 0.059 \text{ pH} + E^{\circ}_{\text{SCE}}$). The working electrodes were prepared as follows: 6 mg of as-prepared catalyst and 3 mg of commercial carbon black powder were homogeneously dispersed in 400 μL of isopropanol and 100 μL of a 5 wt% Nafion solution by ultra-sonication for 30 minutes. Next, 30 μL of the ink was cast atop a clean carbon paper piece and dried under vacuum for 30 minutes resulted in 0.18 mg/cm² catalyst loading. The performance of these as-prepared catalysts for the OER was studied in 1 M KOH solution by using different electrochemical techniques including chronoamperometry, cyclic voltammetry and linear sweep voltammetry (LSV).. The same drop-casting method was used to prepare the samples for the EDX mapping, but casted atop glassy carbon.

Electrochemical Impedance Spectroscopy (EIS) measurements were performed at the onset potential with a disturbance potential of 5 mV and a frequency range from 1 MHz to 0.1 Hz.

Tafel slopes were calculated from the LSV curves by plotting the potential against log (current density). Chronopotentiometry measurements were done in 1 M KOH at three different current densities, typically 5 and 10 mA cm⁻², to investigate the long-term stability of the catalysts (catalyst loading $\sim 0.1 \text{ mg/cm}^2$). The electrochemically active surface area (ECSA) was estimated from the double-layer capacitance (C_{dl}) obtained from the CVs in the non-Faradaic region of applied potential with various scan rates. The C_{dl} values were calculated from the slope of the $\Delta I = I_{\text{anodic}} - I_{\text{cathodic}}$ versus the scan rate plot. The relative ECSA was then estimated by dividing the C_{dl} of the substrate (carbon

paper, CP) coated with ink loaded with the catalyst materials (CuS and CuCo₂S₄), with the C_{dl} of the substrate coated with ink that does not contain any catalyst material.

2. Results and Discussion

2.1. Morphology and Crystal Phase of CuS Microflowers

The effect of synthesis parameters including reaction time and temperature on the morphology and crystallography of the obtained CuS particles was first examined by scanning electron microscopy (SEM) and X-ray diffraction (XRD) to draw a relation between the synthesis parameters and the structure and shape of the obtained materials.

To study the effect of the reaction temperature on the obtained CuS particles, CuS particles were created at various reaction temperatures (120-200 °C) at fixed reaction time (1 hour). Figure 1 shows the respective SEM images and XRD patterns of the resulting CuS particles. As clearly seen in Figure 1 a-f (SEM images), the morphology of the obtained CuS particles is significantly affected by the reaction temperature. At 120 °C, highly aggregated particles with irregular shapes are observed, while at 140 °C, a dense mat of interlaced elongated features composed of highly aggregated flake-like particles is obtained. As a result, it is hard to estimate the actual average particle sizes of these flakes, however the size of its primary rod- or flake- like features is ~2 μm. At 160 °C, these CuS flakes were hierarchically arranged in flower-like microstructures with 2 μm diameter and their primary building units (the flakes) are on the order of 1.5 μm. The shape of the roughly spherical aggregates resembles desert rose crystals with highly intersected individual flake-like plates, although of course on a much smaller length scale. Moreover, CuS particles with a rather diverse set of shapes were obtained at higher reaction temperatures (170 °C). Where some of them exhibited pretty similar morphologies to that of the created CuS particles at 140 or 160 °C, while others showed “stack of pancakes” morphology similar to that of the ZnO.⁵⁷

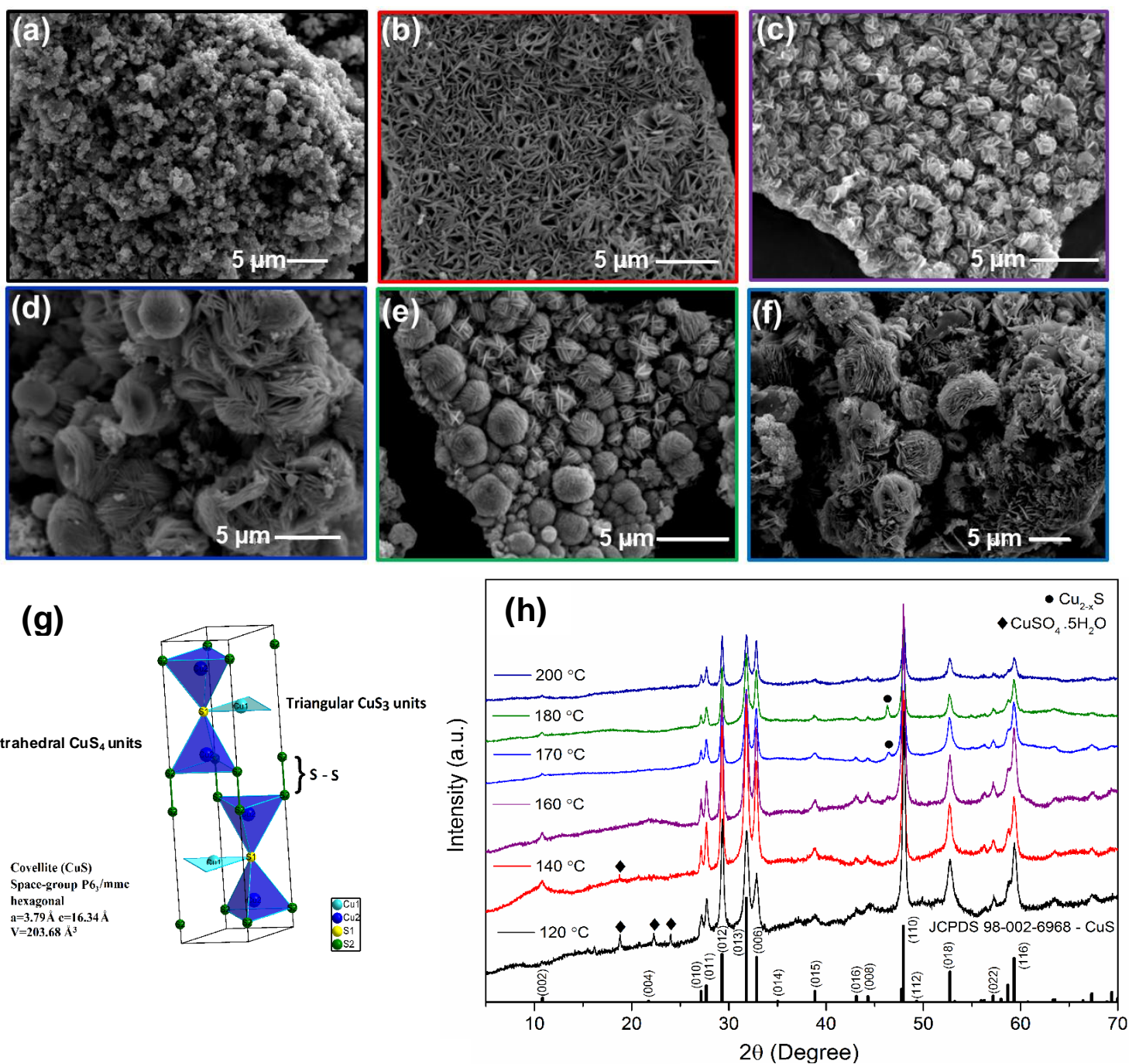


Figure 1. (a-f) SEM images of the obtained CuS particles at different reaction temperatures. (a) 120 °C, (b) 140 °C, (c) 160 °C, (d) 170 °C, (e) 180 °C, and (f) 200 °C using an identical reaction time of 1 hour. (g) Structure of covellite CuS. Atomic coordinates from Evans and Konnert⁵⁸ drawing with diamond. (h) XRD patterns of the synthesized CuS particles at different temperatures (same color code as in Figure 1(a-f)).

Additionally, SEM images of these samples indeed indicate that the observed roughly spherical particles are composed of plate-like particles rather than rod-like ones. Finally, the sizes of these roughly spherical aggregates are quite larger ($\sim 4 \mu\text{m}$) and seem to have a broader size distribution. Once More, this is challenging to estimate attributing to the high degree of aggregation in these materials.

Even using further higher reaction temperatures ($180 \text{ }^\circ\text{C}$) yield CuS particles with different set of morphologies, mostly flower-like microstructures, analogous to those obtained at $160 \text{ }^\circ\text{C}$. Besides, some ball-like particles with average diameter of $3 \mu\text{m}$ are also observed. At $200 \text{ }^\circ\text{C}$, CuS particles with “stack of pancakes” morphologies are seen again with building units having a similar dimension as before, but with much lower degree of morphological order and homogeneity than the synthesized materials at lower temperature.

The covellite (CuS) structure has a rich atomic environment consisting of Cu-S layers linked by S-S covalent bonds. Every Cu-S layer consists of a triangular CuS_3 layer sandwiched between two layers of tetrahedral CuS_4 , Figure 1(g). Figure 1(h) displays the corresponding XRD patterns of the created CuS particles at different temperatures. As seen in this figure, all the prepared CuS materials show all typical reflections of the hexagonal structure of the covellite (CuS) phase ($P6_3/mmc$, primitive hexagonal unit cell with $a = b = 3.790$ and $c = 16.340 \text{ \AA}$, JCPDS 98-002-6968). Nevertheless, the obtained CuS particles at lower temperatures (120 and $140 \text{ }^\circ\text{C}$) exhibit additional reflections at $2\theta = 15 - 25^\circ$, which are assigned to impurities (copper sulphate pentahydrate, $\text{CuSO}_4 \cdot 5\text{H}_2\text{O}$, JCPDS 00-011-0646). Samples obtained at $160 \text{ }^\circ\text{C}$ yield patterns that can be assigned to pure hexagonal CuS. The existence of a sharp and strong (110) reflection indicates a preferred orientation of the CuS particles. XRD patterns of the created particles at $170 \text{ }^\circ\text{C}$ and $180 \text{ }^\circ\text{C}$ exhibit extra reflections indexed to Cu_{2-x}S , in addition the typical reflections of the hexagonal CuS phase. The XRD results are in good agreement with literature⁵⁹, where many researchers reported the reversible transformation between covellite CuS

and Cu_{2-x}S at $160\text{ }^\circ\text{C} \leq T \leq 180\text{ }^\circ\text{C}$, while only CuS is exist at lower ($T \leq 160\text{ }^\circ\text{C}$) and higher ($T \geq 180\text{ }^\circ\text{C}$) temperatures.

With a further rise of the reaction temperature to $200\text{ }^\circ\text{C}$, the obtained CuS particles show pure hexagonal CuS (JCPDS 98-002-6968) again as clearly seen from their obtained XRD patterns, consistent with literature.⁵⁹ Concluding from the XRD results, the grown samples at $160\text{ }^\circ\text{C}$ showed pure covellite CuS phase with a high crystallinity indicating that these materials would be promising candidates for further investigation, thanks to their crystallographic and morphological homogeneity. The estimated crystallite size of these materials using Scherrer's equation is 25 nm (see experimental part for details). The effect of temperature can possibly be assigned to the formation of microscopic structures in the IL even in the (isotropic) liquid phase, but a more detailed study is currently underway to confirm this hypothesis^{9, 60-61}.

Besides reaction temperature, the effect of reaction time was also studied. Figure 2 shows SEM images of the synthesized CuS microstructures at constant synthesis temperature ($160\text{ }^\circ\text{C}$) for various reaction times, and their respective XRD patterns. A reaction temperature of $160\text{ }^\circ\text{C}$ was chosen since the above shown data reveal that the most clearly defined particle morphologies are produced at $160\text{ }^\circ\text{C}$. Overall, the desert rose crystals-like particles are composed of intertwined micrometer-sized flakes (Figure 2a). SEM obviously shows that the reaction time has a considerable effect on the obtained particle morphologies as well as the individual flake sizes. The size distribution of the flakes and the aggregates appears rather narrow, but as the individual particles are highly aggregated, thus the exact estimation of the size distribution is difficult. Longer reaction times result in changes in the morphologies of the precipitates. For instance, reaction time of 4 hours leads to larger, quite densely aggregated, and strongly intersected flake-based ball-like particles with diameters of $2 - 2.5\text{ }\mu\text{m}$ and flake sizes of around $1\text{ }\mu\text{m}$ (Figure 2b). Increasing the reaction time to 6 hours results in the formation of chrysanthemum-like structures with particle sizes between $4 - 5\text{ }\mu\text{m}$ and flake sizes of around $1\text{ }\mu\text{m}$ (Figure 2c).

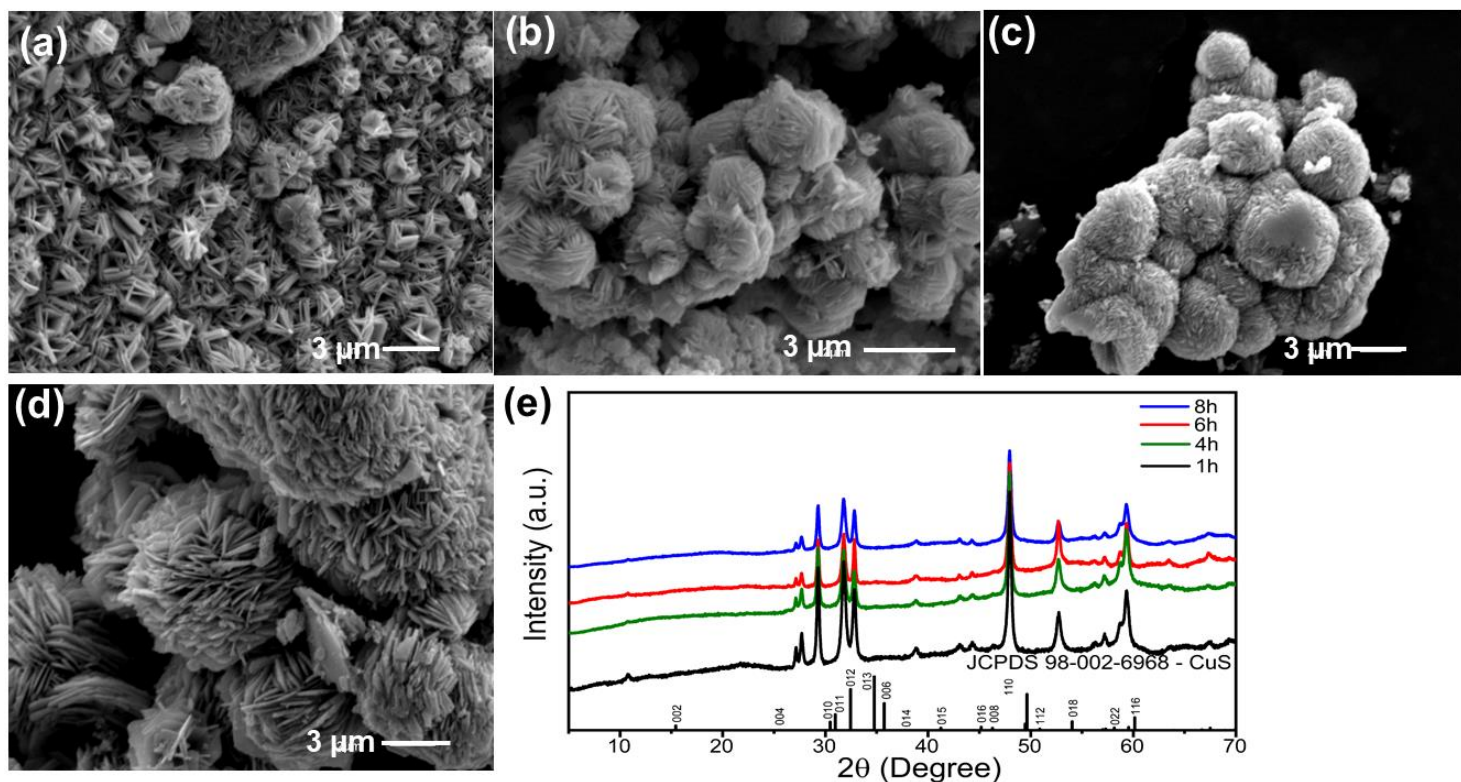


Figure 2. (a-d) SEM images of the synthesized CuS particles at 160 °C at different reaction times; (a) 1 h, (b) 4 h, (c) 6 h, and (d) 8 h. (e) Their respective XRD patterns.

Finally, the obtained hierarchical flower-like microstructures at 8 hours of reaction appear to be composed of well-assembled and closely packed CuS flakes. These flower-like particles have an average diameter of 5 - 5.5 μm with individual flakes with around 1 μm (Figure 2d). Overall, the obtained SEM results suggests that the individual building blocks (i.e. the flakes) of the prepared materials remain roughly the same, but their aggregation (flakes) is strongly affected by the reaction time. Figure S3 and Figure S4 show the TEM images and elemental mapping of CuS particles obtained at 160 °C and 8 hours. It is worth to mention that all the synthesized CuS microstructures at different reaction times show the same diffraction patterns suggesting the formation of hexagonal covellite (Figure 2e).

This confirms the major role of the reaction time and temperature in the assembly of the CuS nanoflakes into different morphologies with less effect on the crystal structure. The morphology of the CuS particles is affected by reaction time because their growth likely occurs via a multistep process, similar to earlier reports on CuCl⁶⁰⁻⁶¹. This also agrees with existing models of crystal growth in complex media, where multiple pathways lead to complex crystal morphologies⁶²⁻⁶³.

2.2. Morphology and Crystal Phase of CuCo₂S₄ Microflowers

In analogy to the above example, CuCo₂S₄ microflowers were synthesized from the ILP [C₄Py]₂[Cu_{0.39}Co_{0.61}Cl₄]. Single crystal structure analysis (see Figures S1 and S2, supporting information for details) of [C₄Py]₂[Cu_{0.39}Co_{0.61}Cl₄] reveals that the structure of the solid ILP is identical to the copper-only compound [C₄Py]₂[CuCl₄].⁵⁰ Once more, (i) the asymmetric unit contains four independent cations and two anions, (ii) the compound crystallizes in the monoclinic space group *P*2₁/*n*, (iii) the crystal structure is stabilized by extended networks of non-classical hydrogen bonds and non-covalent contacts, and (iv) the metal center shows a tetrahedral geometry and is completed by four chloride ligands to afford the anionic [Cu_{0.39}Co_{0.61}Cl₄]²⁻ entity. Moreover, like the two parent compounds [C₄Py]₂[CuCl₄] and [C₄Py]₂[CoCl₄], the mixed metal IL [C₄Py]₂[Cu_{0.39}Co_{0.61}Cl₄] exhibits a glass transition at -37.6 °C, a cold crystallization at 8.6 °C, and a melting transition at 74.7 °C, **Figure S5** (supporting information).

Like in the case discussed before, the ILP [C₄Py]₂[Cu_{0.39}Co_{0.61}Cl₄] can also be reacted with a sulfur source such as (TMS)₂S to yield the respective sulfide. **Figure S6a** shows a representative SEM image and XRD patterns of CuCo₂S₄ particles obtained at 160 °C and 6 h of reaction time. The reason for selecting these reaction conditions is that CuS powders (see section 3.1 above) synthesized under these conditions show the highest OER activity of all CuS materials investigated here (see section 3.3

below, see Figure S9). Indeed, SEM of the CuCo_2S_4 particles shows rather well-defined, but highly aggregated CuCo_2S_4 nanoflakes (with average particle size of ~ 44 nm) with some irregular structures. **Figure S6b** shows the XRD pattern of the CuCo_2S_4 powders in comparison to the pattern obtained from CuS made at identical reaction conditions.

XRD patterns obtained from the solids synthesized from $[\text{C}_4\text{Py}]_2[\text{Cu}_{0.39}\text{Co}_{0.61}\text{Cl}_4]$ show reflections that can be assigned to the cubic phase of carrollite (CuCo_2S_4 , $Fd\bar{3}m$, primitive cubic unit cell with $a = 9.458$ Å, JCPDS 98-003-1107). Additional reflections at $2\theta = 29.8^\circ$ and 52.1° can be assigned to cobaltpentlandite (Co_9S_8 , JCPDS 98-003-1753). All reflections are broad, indicating the formation of nanocrystalline building blocks. Consistent with the XRD analysis, **Figure S6d** shows representative energy dispersive X-ray spectroscopy (EDXS) data that prove the presence of Cu, Co, and S in the powders. Figure S7 and Figure S8 display the TEM, EDS and elemental mapping analysis of CuCo_2S_4 particles. As obviously seen in Figure S7, CuCo_2S_4 exhibited sheet-like structure.

Figure 3a shows a typical XPS survey spectrum showing the presence of Cu, Co, and S in the sample; these data are consistent with EDXS data shown above. The observed Cl and C peaks may originate from some residual IL precursor $[\text{C}_4\text{Py}]_2[\text{Cu}_{0.39}\text{Co}_{0.61}\text{Cl}_4]$, while detected O and C peaks could come from adsorbed O_2 , H_2O , or CO_2 species on the surface of the sample and adventitious hydrocarbon from the XPS instrument.⁶⁴ **Figure 3b** shows the S energy region of the XPS spectrum. The peaks at 161.30 and 162.40 eV can be assigned to $2p_{1/2}$ and $2p_{3/2}$ core levels at S^{2-} . The broad peaks at 168.97 eV can be ascribed to SO_4^{2-} indicating that the sulfur species on the surface is partially oxidized, likely by air.⁶⁵ **Figure 3c** shows the Cu energy region of the XPS spectrum. The $\text{Cu}2p_{3/2}$ and $\text{Cu}2p_{1/2}$ peaks are observed at around 950.97 and 931.20 eV ($\Delta E = 19.75$ eV), respectively. Each peak can be decomposed into two well-defined peaks attributed to Cu^+ and Cu^{2+} .⁶⁶

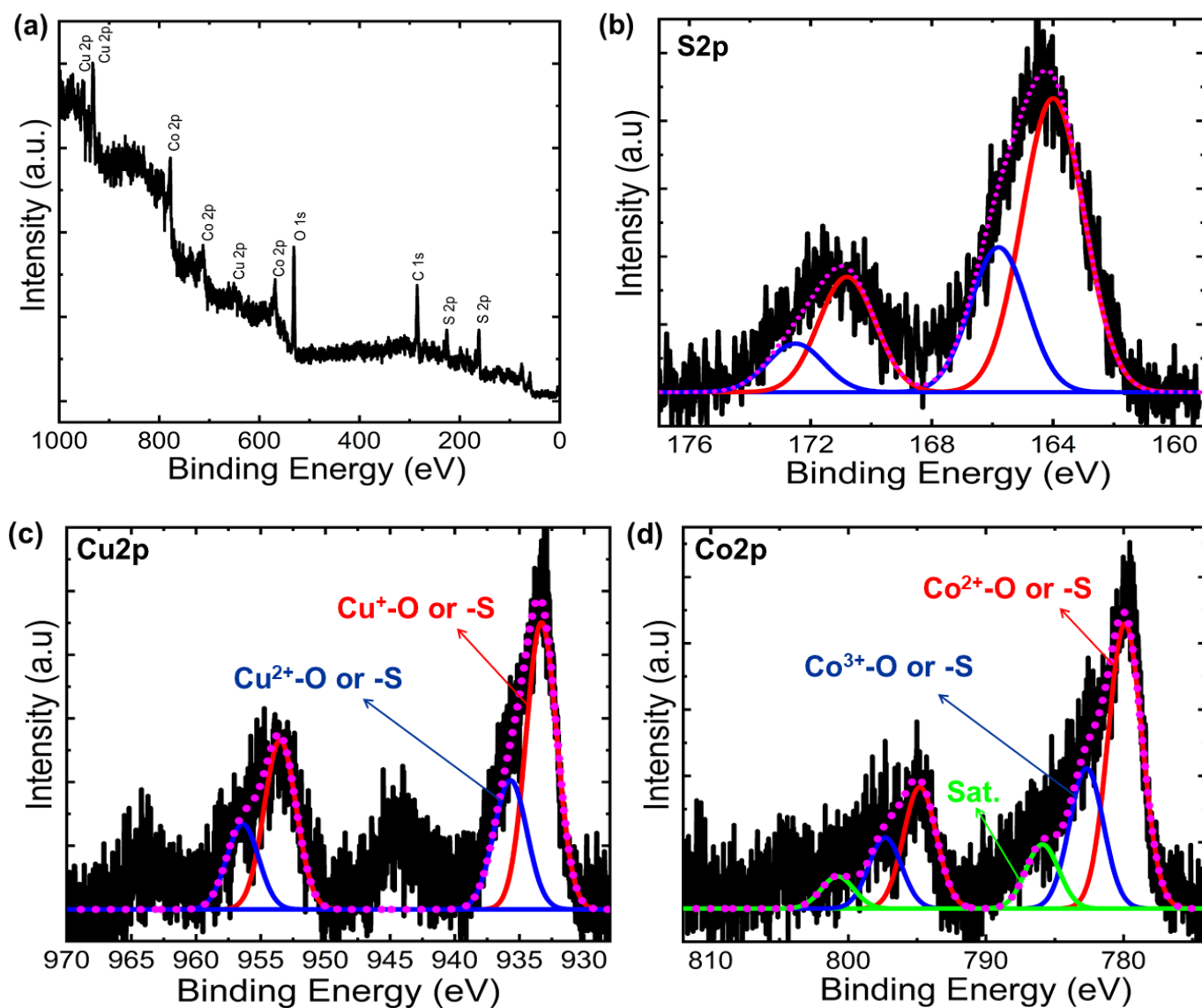


Figure 3. (a) XPS survey spectrum, and high-resolution XPS spectra of (b) S 2p, (c) Cu 2p, and (d) Co 2p regions in the XPS spectra of the CuCo₂S₄ powders.

In the Co 2p region (**Figure 3c**), the binding energy peaks of Co 2p_{1/2} and Co 2p_{3/2} are observed at around 793.09 and 778.09 eV ($\Delta E = 15$ eV) together with their satellites, respectively. The fitted peaks at 780.1 and 782.6 eV are attributed to Co²⁺ and Co³⁺ species, while the peaks at 785 and 788.7 eV can be assigned to Co²⁺ and Co³⁺ species bonded with sulfur. These data clearly show that Cu and Co are both present in the materials.⁶⁷ As a result, XPS analysis demonstrates the presence of Cu²⁺, Co³⁺, and S²⁻. This is in good agreement with literature, where the individual oxidation states in carrollite are generally shown as Cu²⁺Co³⁺S₄²⁻ to comply with charge balance.⁶⁸ However, XPS further shows that Cu⁺ and Co²⁺ are also present in the materials; this is an important factor for the OER, see below.

2.3. Oxygen Evolution Reaction (OER)

The electrocatalytic performance of the carrollite CuCo₂S₄ catalyst towards the OER was investigated in 1.0 M KOH aqueous solution using a standard three-electrode setup. For comparison, analogous measurements were performed with the CuS powders described above (section 3.1), with commercial Pt/C (20 wt%) and IrO₂ catalysts, and with pristine carbon paper. The same mass loadings were used for all catalysts.

Figure 4 clearly shows that the as-prepared mixed metal thiospinel (CuCo₂S₄) microflowers exhibit an excellent performance (in terms of stability and activity) for driving OER. Figures 4a and b clearly show that the CuCo₂S₄ microflowers have the best OER catalytic activity with the lowest OER onset potential (1.345 V vs RHE, the required potential to achieve 2.5 mA cm⁻²) together with the smallest required overpotential (0.23 V) to achieve a current density of 10 mA/cm² among the investigated catalyst materials. The higher electrocatalytic activity of the CuCo₂S₄ catalyst is also evidenced from the lower obtained potential at certain current density (**Fig. 4b**) and larger current density obtained at fixed potential (**Figure 4c**).

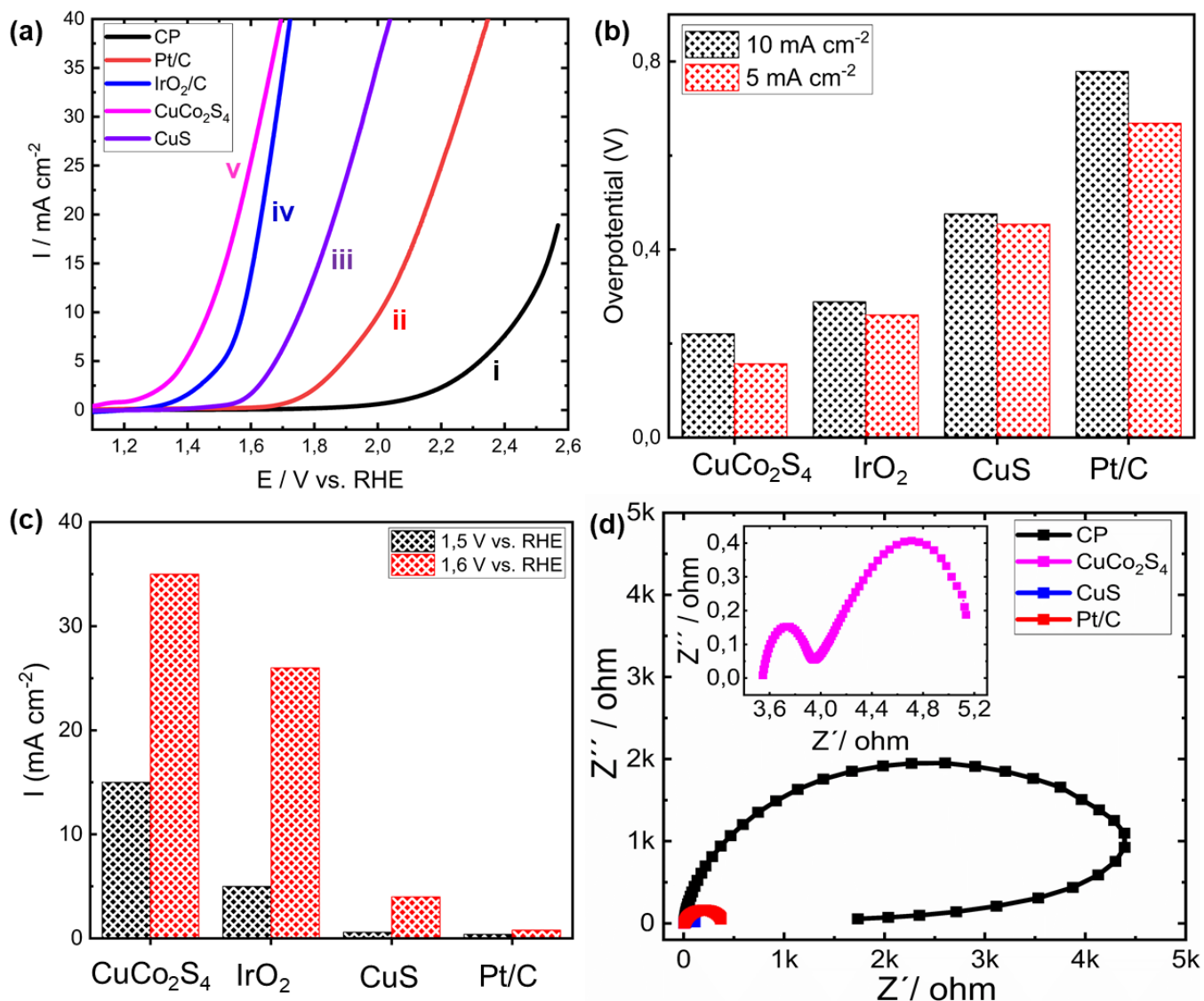


Figure 4. OER performance in 1.0 M KOH (a) Polarization curves of bare CP (i, black-curve), Pt/C@CP (ii, red-curve), $\text{CuS}_{\text{flowers}}@CP$ (iii, violet-curve), $\text{IrO}_2@CP$ (iv, blue-curve) and $\text{CuCo}_2\text{S}_4@CP$ (v, pink-curve). Potential scan rate = 5 mV/s. (b) required potential (upper-plot) and overpotential (lower-plot) for 5 and 10 mA cm^{-2} . (c) obtained current densities at 1.5 and 1.6 V vs. RHE (d) Nyquist plots of bare CP (a), Pt/C@CP, $\text{CuS}_{\text{flowers}}@CP$ and $\text{CuCo}_2\text{S}_4@CP$. Same color-coding are used in Fig. 4d as in Fig. 4a.

As shown in **Figure 4c**, CuCo_2S_4 catalyst showed 14.8 mA/cm^2 at $\sim 1.5 \text{ mV}$ (vs. RHE) which is ~ 3 , ~ 30 , and ~ 75 times higher compared to commercial IrO_2 , undoped CuS flowers, and Pt/C electrodes, respectively.

The as-synthesized CuCo_2S_4 powders exhibit a higher activity than those of many previously reported Cu-based electrodes including oxides, sulfides, and Co-Cu alloys, see Table S5. Compared to the CuCo_2S_4 microflowers, the as-synthesized CuS microflowers show a higher OER onset potential ($\sim 1.63 \text{ V}$ vs. RHE) associated with very high potential to obtain 10 mA/cm^2 . This is surprising because the CuS powder exhibiting a ca. 1.7 times larger roughness (as estimated using the double-layer capacitance, C_{dl}) than the corresponding CuCo_2S_4 powders, see **Figure S10**. The higher electrochemically active surface area of the CuS microflowers compared to CuCo_2S_4 is attributed to the flower-like morphologies of CuS in contrast to CuCo_2S_4 , which has a rather poor and micron-scale morphology with a less open surface, see **Figure S6-8**.

Figure S6 shows Tafel slopes of the as synthesized electrocatalyst materials as calculated by using the results shown in Figure 3a. Figure S11 shows that CuCo_2S_4 and CuS microflowers have Tafel slopes of 211 and 157 mV/dec, respectively.

Why does the CuCo_2S_4 catalyst with 2-fold lower ECSA exhibit higher activity compared to CuS flower-like structures? The presence of cobalt is believed to improve OER activity via reducing the charge transfer resistance together with their synergistic and electronic effects as indicated from EIS and XPS measurements. EIS measurements have been measured at the prepared electrocatalyst materials (CuS and CuCo_2S_4 microflowers) in order to determine the origin of enhanced performance of CuCo_2S_4 for OER. **Figure 4d** displays the Nyquist plots of the bare and modified carbon papers with Pt/C, CuS and CuCo_2S_4 nanostructures. The figure clearly illustrates that the presence of cobalt significantly

decreasing the OER charge transfer resistance, where CuCo_2S_4 shows a much lower charge transfer resistance ($\sim 1,6 \Omega$) compared to CuS flowers ($\sim 21 \Omega$) and commercial Pt/C electrode ($\sim 4 \text{ K}\Omega$).

The CuCo_2S_4 exhibit outstanding long-term stability compared to CuS flowers and commercial Pt/C electrode, Figure 5. This excellent stability of the CuCo_2S_4 electrodes is demonstrated by the negligible change in its OER overpotential over 2 hours at current density of 5 and 10 mA cm^{-2} compared to the significant increase of OER potential of both the undoped CuS flowers and Pt/C electrode, as shown in Figure 5a. Figure 5b displays the LSVs of the CuCo_2S_4 and CuS catalysts after measuring chronoamperometry test for various times.

Clearly, CuCo_2S_4 shows a remarkable long-term stability compared to CuS flowers, where CuCo_2S_4 microflowers lose only $\sim 15\%$ of their initial activity after 12 hours compared to $\sim 91\%$ loss of the CuS flowers, as estimated using the current loss at 1.78 V vs. RHE . The low stability of the CuS flowers correlates with a large increase in their OER charge transfer resistance with time (Figure 5c).

This increase in the OER charge transfer resistance is thought to originate from the significant decrease of the CuS flowers electrochemically active surface area attributing to the destruction of their unique flower-like structures. On the other hand, the charge transfer resistance of the OER on CuCo_2S_4 (Fig. 5d) remain almost unchanged with long-term repeated OER runs, highlighting the high stability of the CuCo_2S_4 .

3. Conclusion

Carrollite CuCo_2S_4 microflowers were prepared from the ionic liquid precursor (ILP) bis(N-butylpyridinium) tetrachlorido cuprate(II) cobaltate(II), $[\text{C}_4\text{Py}]_2[\text{Cu}_{0.39}\text{Co}_{0.61}\text{Cl}_4]$. The as-prepared CuCo_2S_4 microflowers exhibit outstanding activity and an excellent stability for the oxygen evolution reaction in alkaline medium.

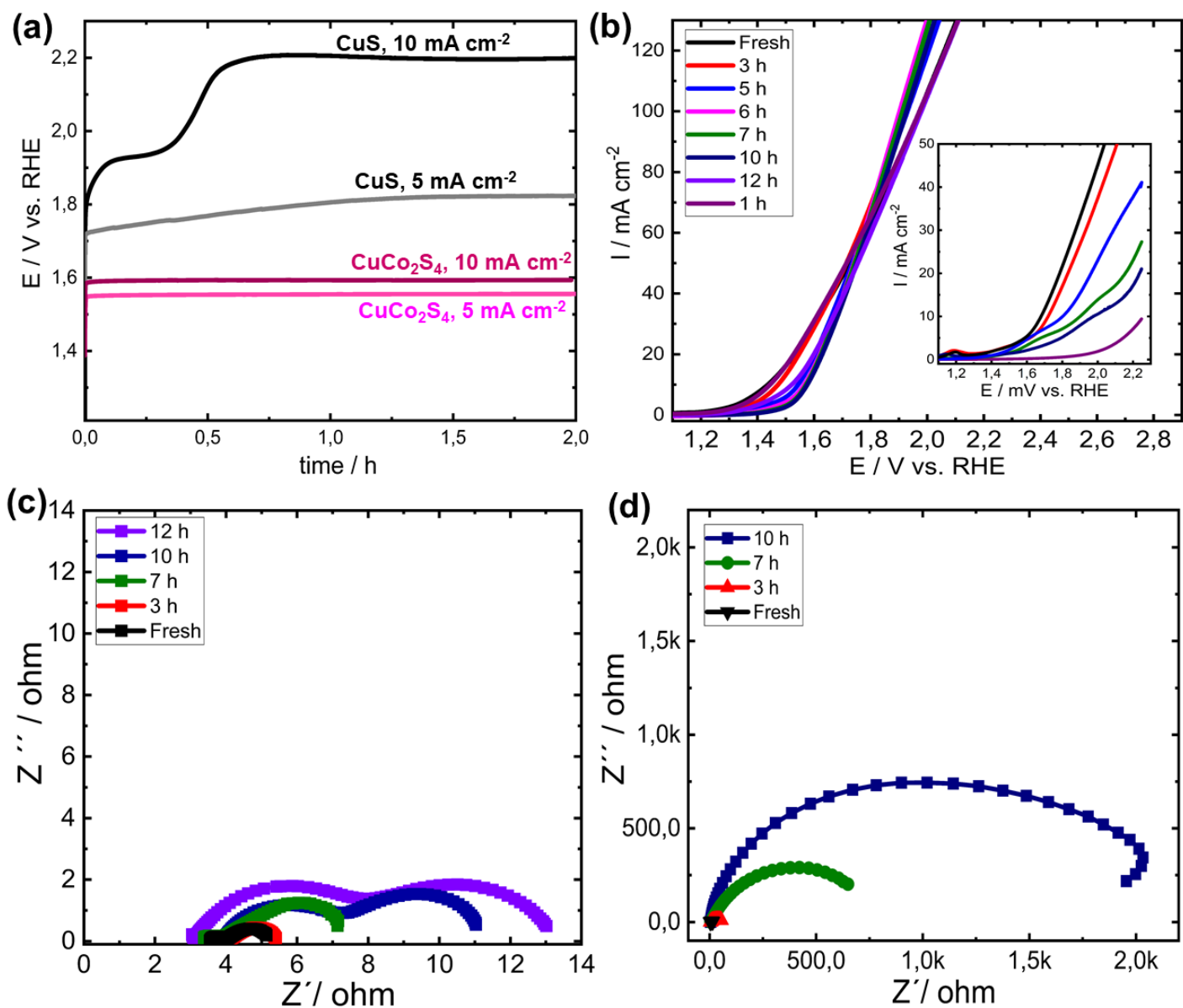


Figure 5. Long-term stability studies in 1 M KOH of CuS flowers and CuCo₂S₄ nanostructures. (a) Long-term durable operation at various current densities (5 and 10 mA/cm²), catalyst loading ~0.1 mg/cm². (b) OER LSVs recorded after measuring chronoamperometry for various times. Inset displays the obtained results at CuS flowers under the same conditions. Same color codes were used for Figure b and its inset. The respective Nyquist plots of Fig. 5b and its inset. Same color codes were used in Fig. 5c and d as in Fig. 5b. (c,d) EIS obtained of CuCo₂S₄ (c) and CuS (d) after measuring OER for different times.

This performance boost is demonstrated by the lower onset potential and higher turnover frequencies of CuCo_2S_4 compared to bare CuS flowers or commercial PtC and IrO_2 electrodes. These performance enhancements of OER are attributed to the presence of Co^{3+} resulting in a significant decrease in the OER charge transfer resistance (reduced from 21 Ω to 5 Ω). Additionally, Co atoms appear to provide Co^{3+} sites, which are useful for the adsorption of different reactive species formed during OER (e.g., OH, O, OOH, etc.).

Acknowledgement

The University of Potsdam and the DFG (projects TA571/13-1 and 13-2, SPP 1708) are thanked for generous financial support. Additional support was provided by Helmholtz-Zentrum Berlin and the Helmholtz Association's Initiative and Networking Fund. The authors acknowledge Sinju Thomas and Ulrike Bloeck from the Department Structure and Dynamics of Energy Materials (EM-ASD), and Katrina Coogan from the Institute of Solar Fuels (EE-IF) in Helmholtz-Zentrum Berlin, for their efforts in conducting the EDX and TEM measurements, respectively.

Supplementary Information. Material characterization of CuS including XRD, SEM and EDS, besides the *Single crystal structure* analysis and TGA of CuCo_2S_4 were provided in the supplementary information. Additionally, the electrochemically active surface area estimation and the performance of the synthesized CuS under different synthesis conditions for OER were presented in the supplementary information.

References

- (1) Chu, S.; Cui, Y.; Liu, N. The Path Towards Sustainable Energy. *Nature materials* **2017**, *16* (1), 16.
- (2) Audichon, T.; Mayousse, E.; Napporn, T. W.; Morais, C.; Comminges, C.; Kokoh, K. B. Elaboration and Characterization of Ruthenium Nano-Oxides for the Oxygen Evolution Reaction in a Proton Exchange Membrane Water Electrolyzer Supplied by a Solar Profile. *Electrochimica Acta* **2014**, *132*, 284-291.
- (3) Lee, Y.; Suntivich, J.; May, K. J.; Perry, E. E.; Shao-Horn, Y. Synthesis and Activities of Rutile IrO₂ and RuO₂ Nanoparticles for Oxygen Evolution in Acid and Alkaline Solutions. *The journal of physical chemistry letters* **2012**, *3* (3), 399-404.
- (4) Roy, N.; Sohn, Y.; Leung, K. T.; Pradhan, D. Engineered Electronic States of Transition Metal Doped TiO₂ Nanocrystals for Low Overpotential Oxygen Evolution Reaction. *The Journal of Physical Chemistry C* **2014**, *118* (51), 29499-29506.
- (5) Gao, M.; Sheng, W.; Zhuang, Z.; Fang, Q.; Gu, S.; Jiang, J.; Yan, Y. Efficient Water Oxidation Using Nanostructured A-Nickel-Hydroxide as an Electrocatalyst. *Journal of the American Chemical Society* **2014**, *136* (19), 7077-7084.
- (6) Trotochaud, L.; Young, S. L.; Ranney, J. K.; Boettcher, S. W. Nickel-Iron Oxyhydroxide Oxygen-Evolution Electrocatalysts: The Role of Intentional and Incidental Iron Incorporation. *Journal of the American Chemical Society* **2014**, *136* (18), 6744-6753.
- (7) Schäfer, H.; Chevrier, D. M.; Zhang, P.; Stangl, J.; Müller - Buschbaum, K.; Hardege, J. D.; Kuepper, K.; Wollschläger, J.; Krupp, U.; Dühnen, S. Electro - Oxidation of Ni₄₂ Steel: A Highly Active Bifunctional Electrocatalyst. *Advanced Functional Materials* **2016**, *26* (35), 6402-6417.
- (8) Schäfer, H.; Küpper, K.; Schmidt, M.; Müller-Buschbaum, K.; Stangl, J.; Daum, D.; Steinhart, M.; Schulz-Kölbel, C.; Han, W.; Wollschläger, J. Steel-Based Electrocatalysts for Efficient and Durable Oxygen Evolution in Acidic Media. *Catalysis Science & Technology* **2018**, *8* (8), 2104-2116.
- (9) Taubert, A. CuCl Nanoplatelets from an Ionic Liquid-Crystal Precursor. *Angewandte Chemie International Edition* **2004**, *43* (40), 5380-5382.
- (10) Göbel, R.; Xie, Z.-L.; Neumann, M.; Günter, C.; Löbbicke, R.; Kubo, S.; Titirici, M.-M.; Giordano, C.; Taubert, A. Synthesis of Mesoporous Carbon/Iron Carbide Hybrids with Unusually High Surface Areas from the Ionic Liquid Precursor [Bmim][FeCl₄]. *CrystEngComm* **2012**, *14* (15), 4946-4951.
- (11) Taubert, A.; Li, Z. Inorganic Materials from Ionic Liquids. *Dalton Transactions* **2007**, (7), 723-727.
- (12) Kim, Y.; Heyne, B.; Abouserie, A.; Pries, C.; Ippen, C.; Günter, C.; Taubert, A.; Wedel, A. Cu Nanoplates from Ionic Liquid Precursors—Application in Organic Photovoltaic Cells. *The Journal of Chemical Physics* **2018**, *148* (19), 193818-193828.
- (13) Duan, X.; Ma, J.; Lian, J.; Zheng, W. The Art of Using Ionic Liquids in the Synthesis of Inorganic Nanomaterials. *CrystEngComm* **2014**, *16* (13), 2550-2559.
- (14) Dobbs, W.; Suisse, J. M.; Douce, L.; Welter, R. Electrodeposition of Silver Particles and Gold Nanoparticles from Ionic Liquid - Crystal Precursors. *Angewandte Chemie International Edition* **2006**, *45* (25), 4179-4182.
- (15) Paraknowitsch, J. P.; Zhang, J.; Su, D.; Thomas, A.; Antonietti, M. Ionic Liquids as Precursors for Nitrogen - Doped Graphitic Carbon. *Advanced Materials* **2010**, *22* (1), 87-92.

- (16) Zhao, L.; Hu, Y. S.; Li, H.; Wang, Z.; Chen, L. Porous Li₄Ti₅O₁₂ Coated with N - Doped Carbon from Ionic Liquids for Li - Ion Batteries. *Advanced Materials* **2011**, *23* (11), 1385-1388.
- (17) Migowski, P.; Machado, G.; Texeira, S. R.; Alves, M. C.; Morais, J.; Traverse, A.; Dupont, J. Synthesis and Characterization of Nickel Nanoparticles Dispersed in Imidazolium Ionic Liquids. *Physical Chemistry Chemical Physics* **2007**, *9* (34), 4814-4821.
- (18) Alammari, T.; Shekhah, O.; Wohlgemuth, J.; Mudring, A.-V. Ultrasound-Assisted Synthesis of Mesoporous B-Ni (OH)₂ and NiO Nano-Sheets Using Ionic Liquids. *Journal of Materials Chemistry* **2012**, *22* (35), 18252-18260.
- (19) Khare, V.; Kraupner, A.; Mantion, A.; Jelacic, A.; Thunemann, A. F.; Giordano, C.; Taubert, A. Stable Iron Carbide Nanoparticle Dispersions in [Emim][Scn] and [Emim][N(CN)₂] Ionic Liquids. *Langmuir* **2010**, *26* (13), 10600-10605.
- (20) Li, Z.; Li, Y.; Luan, Y.; Li, J.; Song, A. In (OH)₃ Particles from an Ionic Liquid Precursor and Their Conversion to Porous In₂O₃ Particles for Enhanced Gas Sensing Properties. *CrystEngComm* **2013**, *15* (9), 1706-1714.
- (21) Li, R.; Luan, Y.; Zou, H.; Du, J.; Mu, T.; Li, Z. Synthesis and Gas-Sensing Properties of ZnO Particles from an Ionic Liquid Precursor. *RSC advances* **2012**, *2* (7), 3049-3056.
- (22) Li, R.; Du, J.; Luan, Y.; Xue, Y.; Zou, H.; Zhuang, G.; Li, Z. Ionic Liquid Precursor-Based Synthesis of CuO Nanoplates for Gas Sensing and Amperometric Sensing Applications. *Sensors and Actuators B: Chemical* **2012**, *168*, 156-164.
- (23) Vanhoutte, G.; Hojniak, S. D.; Bardé, F.; Binnemans, K.; Fransaer, J. Fluorine-Functionalized Ionic Liquids with High Oxygen Solubility. *RSC Advances* **2018**, *8* (9), 4525-4530.
- (24) Rauber, D.; Heib, F.; Dier, T.; Volmer, D. A.; Hempelmann, R.; Schmitt, M. On the Physicochemical and Surface Properties of 1-Alkyl 3-Methylimidazolium Bis (Nonafluorobutylsulfonyl) Imide Ionic Liquids. *Colloids and Surfaces A: Physicochemical and Engineering Aspects* **2017**, *529*, 169-177.
- (25) Kirchhecker, S.; Tröger-Müller, S.; Bake, S.; Antonietti, M.; Taubert, A.; Esposito, D. Renewable Pyridinium Ionic Liquids from the Continuous Hydrothermal Decarboxylation of Furfural-Amino Acid Derived Pyridinium Zwitterions. *Green Chemistry* **2015**, *17* (8), 4151-4156.
- (26) Hou, X.-D.; Smith, T. J.; Li, N.; Zong, M.-H. Novel Renewable Ionic Liquids as Highly Effective Solvents for Pretreatment of Rice Straw Biomass by Selective Removal of Lignin. *Biotechnology and Bioengineering* **2012**, *109* (10), 2484-2493.
- (27) Tröger-Müller, S.; Brandt, J.; Antonietti, M.; Liedel, C. Green Imidazolium Ionics—from Truly Sustainable Reagents to Highly Functional Ionic Liquids. *Chemistry – A European Journal* **2017**, *23* (49), 11810-11817.
- (28) Grozdanov, I.; Najdoski, M. Optical and Electrical Properties of Copper Sulfide Films of Variable Composition. *Journal of Solid State Chemistry* **1995**, *114* (2), 469-475.
- (29) Zhao, Y.; Pan, H.; Lou, Y.; Qiu, X.; Zhu, J.; Burda, C. Plasmonic Cu₂-X S Nanocrystals: Optical and Structural Properties of Copper-Deficient Copper (I) Sulfides. *Journal of the American Chemical Society* **2009**, *131* (12), 4253-4261.
- (30) Lai, C.-H.; Huang, K.-W.; Cheng, J.-H.; Lee, C.-Y.; Hwang, B.-J.; Chen, L.-J. Direct Growth of High-Rate Capability and High Capacity Copper Sulfide Nanowire Array Cathodes for Lithium-Ion Batteries. *Journal of Materials Chemistry* **2010**, *20* (32), 6638-6645.
- (31) Wang, F.; Shifa, T. A.; Zhan, X.; Huang, Y.; Liu, K.; Cheng, Z.; Jiang, C.; He, J. Recent Advances in Transition-Metal Dichalcogenide Based Nanomaterials for Water Splitting. *Nanoscale* **2015**, *7* (47), 19764-19788.

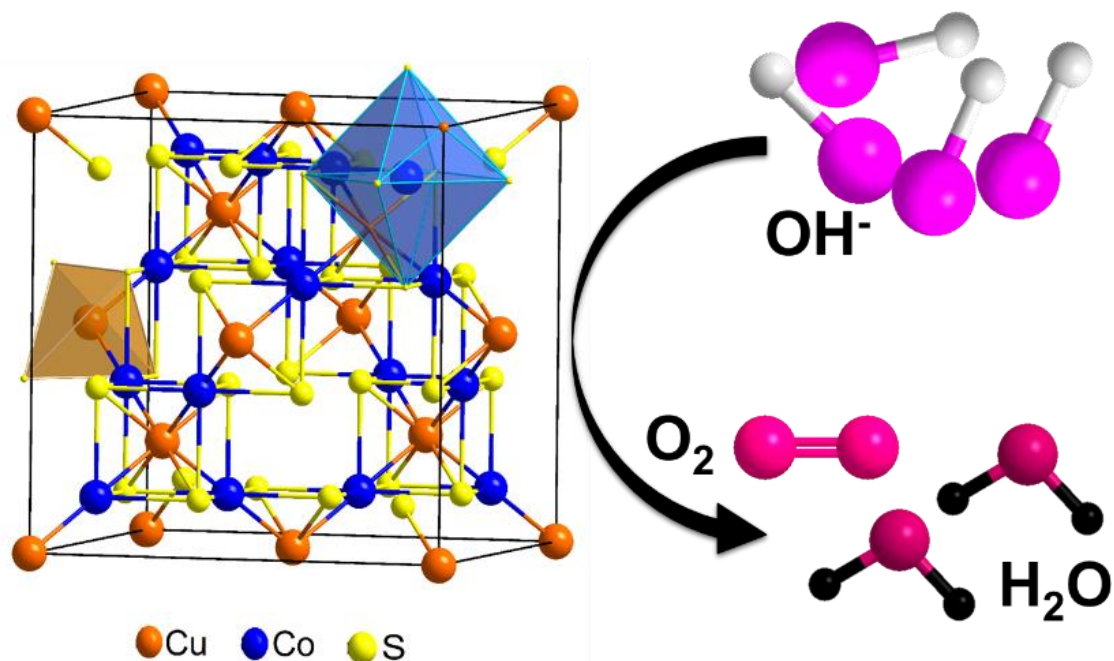
- (32) Feng, C.; Zhang, L.; Wang, Z.; Song, X.; Sun, K.; Wu, F.; Liu, G. Synthesis of Copper Sulfide Nanowire Bundles in a Mixed Solvent as a Cathode Material for Lithium-Ion Batteries. *Journal of Power Sources* **2014**, *269*, 550-555.
- (33) Su, Q.; Xie, J.; Zhang, J.; Zhong, Y.; Du, G.; Xu, B. In Situ Transmission Electron Microscopy Observation of Electrochemical Behavior of CoS₂ in Lithium-Ion Battery. *ACS applied materials & interfaces* **2014**, *6* (4), 3016-3022.
- (34) Huang, S.; Liu, J.; He, Q.; Chen, H.; Cui, J.; Xu, S.; Zhao, Y.; Chen, C.; Wang, L. Smart Cu_{1.75}S Nanocapsules with High and Stable Photothermal Efficiency for NIR Photo-Triggered Drug Release. *Nano Research* **2015**, *8* (12), 4038-4047.
- (35) Tian, Q.; Jiang, F.; Zou, R.; Liu, Q.; Chen, Z.; Zhu, M.; Yang, S.; Wang, J.; Wang, J.; Hu, J. Hydrophilic Cu₉S₅ Nanocrystals: A Photothermal Agent with a 25.7% Heat Conversion Efficiency for Photothermal Ablation of Cancer Cells in Vivo. *ACS Nano* **2011**, *5* (12), 9761-9771.
- (36) Farhadyar, N.; Sadjadi, M. S.; Farhadyar, F.; Farhadyar, A. Wet Chemistry Synthesis of Semiconductor Gold/Cu_{1.96}S Nanorod and Study of Its Photoluminescence Properties. *Journal of Nano Research* **2013**, *21*, 51-56.
- (37) Wang, Y.; Hu, Y.; Zhang, Q.; Ge, J.; Lu, Z.; Hou, Y.; Yin, Y. One-Pot Synthesis and Optical Property of Copper(I) Sulfide Nanodisks. *Inorganic Chemistry* **2010**, *49* (14), 6601-6608.
- (38) Wang, H.; Zhang, J.-R.; Zhao, X.-N.; Xu, S.; Zhu, J.-J. Preparation of Copper Monosulfide and Nickel Monosulfide Nanoparticles by Sonochemical Method. *Materials Letters* **2002**, *55* (4), 253-258.
- (39) Gorai, S.; Ganguli, D.; Chaudhuri, S. Synthesis of Copper Sulfides of Varying Morphologies and Stoichiometries Controlled by Chelating and Nonchelating Solvents in a Solvothermal Process. *Crystal Growth & Design* **2005**, *5* (3), 875-877.
- (40) Gao, M.-R.; Xu, Y.-F.; Jiang, J.; Yu, S.-H. Nanostructured Metal Chalcogenides: Synthesis, Modification, and Applications in Energy Conversion and Storage Devices. *Chemical Society Reviews* **2013**, *42* (7), 2986-3017.
- (41) Lewis, A. E. Review of Metal Sulphide Precipitation. *Hydrometallurgy* **2010**, *104* (2), 222-234.
- (42) Li, Q.; Wang, X.; Tang, K.; Wang, M.; Wang, C.; Yan, C. Electronic Modulation of Electrocatalytically Active Center of Cu₇S₄ Nanodisks by Cobalt-Doping for Highly Efficient Oxygen Evolution Reaction. *ACS nano* **2017**, *11* (12), 12230-12239.
- (43) Chauhan, M.; Reddy, K. P.; Gopinath, C. S.; Deka, S. Copper Cobalt Sulfide Nanosheets Realizing a Promising Electrocatalytic Oxygen Evolution Reaction. *ACS Catalysis* **2017**, *7* (9), 5871-5879.
- (44) Liu, Y.; Xiao, C.; Lyu, M.; Lin, Y.; Cai, W.; Huang, P.; Tong, W.; Zou, Y.; Xie, Y. Ultrathin Co₃S₄ Nanosheets That Synergistically Engineer Spin States and Exposed Polyhedra That Promote Water Oxidation under Neutral Conditions. *Angewandte Chemie* **2015**, *127* (38), 11383-11387.
- (45) Tang, J.; Ge, Y.; Shen, J.; Ye, M. Facile Synthesis of Cu₂S₄ as a Novel Electrode Material for Ultrahigh Supercapacitor Performance. *Chemical Communications* **2016**, *52* (7), 1509-1512.
- (46) Wiltrout, A. M.; Read, C. G.; Spencer, E. M.; Schaak, R. E. Solution Synthesis of Thiospinel Cu₂S₄ Nanoparticles. *Inorganic chemistry* **2015**, *55* (1), 221-226.
- (47) Ma, Z.; Yu, J.; Dai, S. Preparation of Inorganic Materials Using Ionic Liquids. *Advanced Materials* **2010**, *22* (2), 261-285.
- (48) Li, Z.; Khimyak, Y. Z.; Taubert, A. Lessons from a "Failed" Experiment: Zinc Silicates with Complex Morphology by Reaction of Zinc Acetate, the Ionic Liquid Precursor (Ilp) Tetrabutylammonium Hydroxide (Tbah), and Glass. *Materials* **2008**, *1* (1), 3-24.

- (49) Thiel, K.; Klamroth, T.; Strauch, P.; Taubert, A. On the Interaction of Ascorbic Acid and the Tetrachlorocuprate Ion [CuCl₄]²⁻ in CuCl Nanoplatelet Formation from an Ionic Liquid Precursor (Ilp). *Physical Chemistry Chemical Physics* **2011**, *13* (30), 13537-13543.
- (50) Abouserie, A.; Zehbe, K.; Metzner, P.; Kelling, A.; Günter, C.; Schilde, U.; Strauch, P.; Körzdörfer, T.; Taubert, A. Alkylpyridinium Tetrahalidometallate Ionic Liquids and Ionic Liquid Crystals: Insights into the Origin of Their Phase Behavior. *European Journal of Inorganic Chemistry* **2017**, *2017* (48), 5640-5649.
- (51) X-Area (Stoe 2015).
- (52) Sheldrick, G. Shelxs-2013/1, Program for the Solution of Crystal Structures. *Institute for Inorganic Chemistry, University of Göttingen, Göttingen, Germany* **2013**.
- (53) Sheldrick, G. Shelxs-2014/7 and Shelxl-2014/7 Program for Solution and Refinement of Crystal Structures. *Institute for Inorganic Chemistry, University of Göttingen, Göttingen, Germany* **2014**.
- (54) Pennington, W. T. Diamond–Visual Crystal Structure Information System. *Journal of Applied Crystallography* **1999**, *32* (5), 1028-1029.
- (55) Farrugia, L. J. Ortep-3 for Windows-a Version of Ortep-ii with a Graphical User Interface (Gui). *Journal of Applied Crystallography* **1997**, *30* (5), 565-565.
- (56) Birks, L.; Friedman, H. Particle Size Determination from X - Ray Line Broadening. *Journal of Applied Physics* **1946**, *17* (8), 687-692.
- (57) Taubert, A.; Palms, D.; Weiss, Ö.; Piccini, M.-T.; Batchelder, D. N. Polymer-Assisted Control of Particle Morphology and Particle Size of Zinc Oxide Precipitated from Aqueous Solution. *Chemistry of Materials* **2002**, *14* (6), 2594-2601.
- (58) Evans, H.; Konnert, J. Crystal Structure Refinement of Covellite. *Am. Mineral* **1976**, *61* (9-10), 996-1000.
- (59) Liu, Y.; Liu, M.; Swihart, M. T. Reversible Crystal Phase Interconversion between Covellite Cus and High Chalcocite Cu₂s Nanocrystals. *Chemistry of Materials* **2017**, *29*(11), 4783–4791.
- (60) Taubert, A.; Steiner, P.; Manton, A. Ionic Liquid Crystal Precursors for Inorganic Particles: Phase Diagram and Thermal Properties of a CuCl Nanoplatelet Precursor. *The Journal of Physical Chemistry B* **2005**, *109* (32), 15542-15547.
- (61) Taubert, A.; Palivan, C.; Casse, O.; Gozzo, F.; Schmitt, B. Ionic Liquid-Crystal Precursors (Ilcps) for CuCl Platelets: The Origin of the Exothermic Peak in the Dsc Curves. *The Journal of Physical Chemistry C* **2007**, *111* (11), 4077-4082.
- (62) Cölfen, H.; Mann, S. Higher-Order Organization by Mesoscale Self-Assembly and Transformation of Hybrid Nanostructures. *Angewandte Chemie International Edition* **2003**, *42* (21), 2350-2365.
- (63) Cölfen, H.; Antonietti, M. Mesocrystals: Inorganic Superstructures Made by Highly Parallel Crystallization and Controlled Alignment. *Angewandte Chemie International Edition* **2005**, *44* (35), 5576-5591.
- (64) Yu, J.; Hai, Y.; Cheng, B. Enhanced Photocatalytic H₂-Production Activity of TiO₂ by Ni (OH)₂ Cluster Modification. *The Journal of Physical Chemistry C* **2011**, *115* (11), 4953-4958.
- (65) Nie, L.; Wang, H.; Liu, S.; Yuan, R. Solvothermal Synthesis of CuCo₂S₄ Nanoparticles for Rechargeable Lithium-Ion Battery Anodes. *Chalcogenide Letters* **2016**, *13* (12), 555-562.
- (66) Zhang, J.; Yu, J.; Zhang, Y.; Li, Q.; Gong, J. R. Visible Light Photocatalytic H₂-Production Activity of Cus/Zns Porous Nanosheets Based on Photoinduced Interfacial Charge Transfer. *Nano Letters* **2011**, *11* (11), 4774-4779.

(67) Hou, L.; Hua, H.; Bao, R.; Chen, Z.; Yang, C.; Zhu, S.; Pang, G.; Tong, L.; Yuan, C.; Zhang, X. Anion - Exchange Formation of Hollow NiCo₂S₄ Nanoboxes from Mesocrystalline Nickel Cobalt Carbonate Nanocubes Towards Enhanced Pseudocapacitive Properties. *ChemPlusChem* **2016**, *81* (6), 557-563.

(68) Patrick, R. A.; Coker, V. S.; Pearce, C. I.; Telling, N. D.; van der Laan, G. The Oxidation State of Copper and Cobalt in Carrollite, CuCo₂S₄. *The Canadian Mineralogist* **2008**, *46* (5), 1317-1322.

Table of Contents



Herein, CuS and CuCo₂S₄ nanostructures were synthesized from single ionic liquid precursors using a novel and highly controllable synthesis strategy. The obtained CuCo₂S₄ showed outstanding activity and stability for oxygen evolution reaction. The morphology was tuned via reaction time and temperature.